Fig. 3B, we calculated the transfer function of the 60-nm half-pitch object for various silver film thicknesses. Assisted by surface plasmon excitation, a maximum enhancement of the selected subwavelength feature was reached for a 35-nm-thick silver slab. Above a thickness of 40 nm, the enhancement was damped by material absorption, destroying the superlensing effect. Such a critical thickness gives a measure for the efficient coupling of the evanescent modes at two interfaces of the silver film. The existence of this critical thickness is in good agreement with our previous finding (*15*).

The silver superlens can also image arbitrary nanostructures with sub–diffraction-limited resolution (Fig. 4). The recorded image "NANO" in Fig. 4B shows that we can faithfully reproduce the fine features from the mask (Fig. 4A) in all directions with good fidelity. As previously discussed, only the scattered TM evanescent waves from the object are coupled into the surface plasmon resonance of the silver film, and they become a primary component for restoring a sub–diffraction-limited image. For comparison, Fig. 4C displays the control experiment performed on the same mask, with "NANO" embedded in 75-nm planarized PMMA. With the same exposure condition, we observed the image of "NANO" with much wider lines, even with the extended development time (>1 min). Because the lines are a few micrometers apart, the subwavelength openings can be treated as isolated line sources, with a broad band of Fourier spectrum: The larger Fourier components decay strongly, and only the smaller Fourier components reach the imaging plane, resulting in a diffraction-limited image as shown in Fig. 4C. In contrast, with a silver superlens, we can resolve an average line width of 89 nm (Fig. 4D), which is much smaller than that of the diffraction-limited image. With natural and structured plasmons (*28–31*) in metals and phonon polaritons in semiconductors, a potential low-loss, high-resolution superlens is achievable.

References and Notes

1. J. B. Pendry, *Phys. Rev. Lett.* **85**, 3966 (2000).
2. H. I. Smith, *Proc. IEEE* **62**, 1361 (1974).
3. U. Ch. Fischer, H. P. Zingsheim, *J. Vac. Sci. Technol.* **19**, 881 (1981).
4. J. G. Goodberlet, H. Kavak, *Appl. Phys. Lett.* **81**, 1315 (2002).
5. X. Luo, T. Ishihara, *Appl. Phys. Lett.* **84**, 4780 (2004).
6. M. C. K. Wiltshire *et al.*, *Science* **291**, 849 (2001).
7. M. C. K. Wiltshire *et al.*, *Opt. Express* **11**, 709 (2003).
8. R. A. Shelby, D. R. Smith, S. Schultz, *Science* **292**, 77 (2001).
9. A. K. Iyer, P. C. Kremer, G. V. Eleftheriades, *Opt. Express* **11**, 696 (2003).
10. A. Grbic, G. V. Eleftheriades, *Phys. Rev. Lett.* **92**, 117403 (2004).
11. T.-J. Yen *et al.*, *Science* **303**, 1494 (2004).
12. S. Linden *et al.*, *Science* **306**, 3531 (2004).
13. C. G. Parazzoli *et al.*, *Phys. Rev. Lett.* **90**, 107401 (2003).
14. A. A. Houck, J. B. Brock, I. L. Chuang, *Phys. Rev. Lett.* **90**, 137401 (2003).
15. D. R. Smith, J. B. Pendry, M. C. K. Wiltshire, *Science* **305**, 788 (2004).
16. P. V. Parimi, W. T. Lu, P. Vodo, S. Sridhar, *Nature* **426**, 404 (2003).
17. Z. Liu, N. Fang, T.-J. Yen, X. Zhang, *Appl. Phys. Lett.* **83**, 5184 (2003).
18. N. Fang, X. Zhang, *Appl. Phys. Lett.* **82**, 161 (2003).
19. D. R. Smith *et al.*, *Appl. Phys. Lett.* **82**, 1506 (2003).
20. D. O. S. Melville, R. J. Blaikie, *J. Vac. Sci. Technol.* **B22**, 3470 (2004).
21. D. O. S. Melville, R. J. Blaikie, *J. Opt.* **A7**, S176 (2005).
22. S. A. Ramakrishna, D. Schurig, D. R. Smith, S. Schultz, J. B. Pendry, *J. Mod. Opt.* **49**, 1747 (2002).
23. N. Fang, Z. Liu, T.-J. Yen, X. Zhang, *Opt. Express* **11**, 682 (2003).
24. In our estimation, an ideal mask was assumed to have perfect binary near-field profiles, but the actual intensity may be influenced by the material and geometries of the subwavelength mask near the superlens. Thus, Fig. 3 should be regarded as a general guideline to the performance of the real system. A more accurate description can be given by full vector electromagnetic simulations of the system, such as in (*21*).
25. The image-recording conditions have been optimized to obtain the best possible image contrast in all experiments in this report. See the details of the control experiment in the supporting material on *Science* Online.
26. E. Loewen, E. Popov, *Diffraction Gratings and Applications* (Marcel Dekker, New York, 1997).
27. To compute the image transfer function presented in Fig. 3, the dielectric constant ($2.3013 + 0.0014i$) of PMMA is taken from the 495PMMA product datasheet (Microchem), the refractive index ($n = 1.6099$) of NFR105G is taken from JSR Micro, and a typical value of $\kappa = 0.003$ is taken into account for the absorption of the photoresist. In the computation, we assume that the photoresist occupies the top half of the space, whereas experimentally the actual photoresist layer thickness is 120 nm. The permittivity of silver ($-2.4012 + 0.2488i$) is taken from (*32*).
28. J. B. Pendry, A. J. Holden, W. J. Stewart, I. Youngs, *Phys. Rev. Lett.* **76**, 4773 (1996).
29. H. J. Lezec *et al.*, *Science* **297**, 820 (2002).
30. T. W. Ebbesen, H. J. Lezec, H. F. Ghaemi, T. Thio, P. A. Wolff, *Nature* **391**, 667 (1998).
31. J. B. Pendry, L. Martín-Moreno, F. J. Garcia-Vidal, *Science* **305**, 847 (2004).
32. P. B. Johnson, R. W. Christy, *Phys. Rev. B* **6**, 4370 (1972).

33. The authors acknowledge support from the Office of Naval Research (ONR)/Defense Advanced Research Projects Agency Multidisciplinary University Research Initiative (MURI) (ONR grant N00014-01-1-0803) and from NSF for the Center for Nanoscale Science and Engineering (grant DMI-0327077).

Supporting Online Material

www.sciencemag.org/cgi/content/full/308/5721/534/DC1
Materials and Methods
Figs. S1 to S5
Table S1

16 December 2004; accepted 14 March 2005
10.1126/science.1108759

Monodisperse Double Emulsions Generated from a Microcapillary Device

A. S. Utada,[1] E. Lorenceau,[1] D. R. Link,[1,2] P. D. Kaplan,[3] H. A. Stone,[1] D. A. Weitz[1,2]

Double emulsions are highly structured fluids consisting of emulsion drops that contain smaller droplets inside. Although double emulsions are potentially of commercial value, traditional fabrication by means of two emulsification steps leads to very ill-controlled structuring. Using a microcapillary device, we fabricated double emulsions that contained a single internal droplet in a core-shell geometry. We show that the droplet size can be quantitatively predicted from the flow profiles of the fluids. The double emulsions were used to generate encapsulation structures by manipulating the properties of the fluid that makes up the shell. The high degree of control afforded by this method and the completely separate fluid streams make this a flexible and promising technique.

Mixing two immiscible fluids produces an emulsion, which is defined as a dispersion of droplets of one fluid in a second fluid. Although they are not in equilibrium, emulsions can be metastable, with the droplets retaining their integrity for extended periods of time if their interface is stabilized by a surfactant. Emulsions play critical roles in many forms of processing and in coatings, foods, and cosmetics (*1*). One common use is to compartmentalize one fluid in a second, which is particularly important for packaging and stabilizing fluids and other active ingredients. Even more control and flexibility for encapsulation can be achieved through the use of double emulsions, which are emulsions with smaller droplets of a third fluid within the larger drops. The intermediate fluid adds an additional barrier that separates the innermost fluid from the outer fluid, or the continuous phase. This makes double emulsions highly desirable for applications in controlled release of substances (*2–4*); separation (*5*); and encapsulation of nutrients and flavors for food additives (*6–8*); and for the control of encapsulation, release, and rheology for personal care products (*4*, *9–11*). Additional flexibility is achieved by controlling the state of the

[1]Division of Engineering and Applied Sciences, [2]Department of Physics, Harvard University, Cambridge, MA 02138, USA. [3]Unilever Skin Global Innovation Center, 40 Merritt Boulevard, Trumbull, CT 06611, USA.

middle fluid, which can be selectively gelled or hardened to create solid capsules (*12*, *13*). These capsules can be used to encapsulate of drugs for targeted delivery and release (*14*–*21*).

Multiple emulsions are typically made in a two-step process, by first emulsifying the inner droplets in the middle fluid, and then undertaking a second emulsification step for the dispersion (*22*). Each emulsification step results in a highly polydisperse droplet distribution, exacerbating the polydispersity of the final double emulsion. Thus, any capsules formed from such double emulsions are, by nature, poorly controlled in both size and structure, and this limits their use in applications that require precise control and release of active materials. Microfluidic techniques can circumvent the vagaries of the bulk emulsification process and can produce more uniform double emulsions (*23*), although the range of drop sizes is limited and the devices require localized surface functionalization to control wettability in order to function. Alternatively, flow focusing of coaxial jets (*24*) can produce uniform coated droplets, but these must be reemulsified into the continuous phase, which is a difficult step that precludes widespread use of this technique. The availability of highly monodisperse double emulsions would not only greatly improve their applicability but would also allow for detailed studies of their stability under more controlled conditions (*25*–*31*).

Here we describe a fluidic device that generates double emulsions in a single step, allowing precision control of the outer and inner drop sizes as well as the number of droplets encapsulated in each larger drop. Our device consists of cylindrical glass capillary tubes nested within a square glass tube. By ensuring that the outer diameter of the round tubes is the same as the inner dimension of the square tube, we achieve good alignment to form a coaxial geometry. The innermost fluid is pumped through a tapered cylindrical capillary tube, and the middle fluid is pumped through the outer coaxial region (Fig. 1A), which forms a coaxial flow at the exit of the tapered tube. The outermost fluid is pumped through the outer coaxial region from the opposite direction, and all fluids are forced through the exit orifice formed by the remaining inner tube (Fig. 1A). This geometry results in hydrodynamic focusing (*24*, *32*) of the coaxial flow. The flow passes through the exit orifice and subsequently ruptures to form drops; however, the coaxial flow can maintain its integrity and generate double emulsion droplets within the collection tube. We were also able to produce single emulsions by removing the tapered inner injection tube. In this geometry, our device is reminiscent of the selective withdrawal technique (*33*). Typical diameters of the exit orifice in our devices range from 20 to 200 μm; however, smaller or larger orifices can also be used, which allows the drop size to be adjusted. For convenience, we used a collection tube whose inner diameter was initially narrow and abruptly widened at a distance equal to one–article diameter downstream. These collection tubes were fabricated by axially heating the end of a cylindrical glass tube; as the glass liquefies, the orifice shrinks. Alternatively, we can use a tapered capillary tube as the collection tube. This can provide additional control, but the alignment of two tapered capillary tubes is more delicate and hence more difficult.

We achieved a high degree of control over the resultant double emulsions, varying the diameters of both the outer and inner drops and the number of inner droplets [supporting online material (SOM) text I and fig. S1]. We can produce uniform double emulsions, in which each drop contains a single internal droplet, creating core-shell structures whose drop diameter and shell thickness can be controlled. For example, we can form drops with extremely thin shells; the ratio of shell thickness to outer drop radius can be as low as 3% (Fig. 1B). Alternatively, we can increase the shell thickness up to about 40% of the drop radius (Fig. 1, C to E). We can also vary the number and size of the internal droplets in the double emulsions (Fig. 1, F and G). A stream of double emulsions, each containing a single internal droplet, is shown in Fig. 1H.

To gain insight into the breakup of a coaxial flow, we first considered the formation of single emulsions. We defined two mechanisms of drop formation for our device geometry: dripping and jetting (*34*, *35*). Dripping produces drops close to the entrance of the collection tube, within a single orifice diameter, analogous to a dripping faucet. Droplets produced by dripping are typically highly monodisperse. In contrast, jetting produces a long jet that extends three or more orifice diameters downstream into the collection tube, where it breaks into drops. The jetting regime is typically quite irregular, resulting in polydisperse droplets whose radii are much greater than that of the jet. Jet formation is caused by the viscous stress of the outer fluid, whose viscosity, η_{OF}, is typically 10 times greater than that of the inner fluids in our experiments. Thus, viscous effects dominate over inertial effects, resulting in a low Reynolds number. The formation of double emulsions is similar to that of single emulsions; however, there are two fluids flowing coaxially, each of which can form drops through either mechanism.

The size distribution of the double emulsions is determined by the breakup mechanism, whereas the number of innermost droplets depends on the relative rates of drop formation of the inner and middle fluids (fig. S1). When the rates are equal, the annulus and core of the coaxial jet break simultaneously, generating a

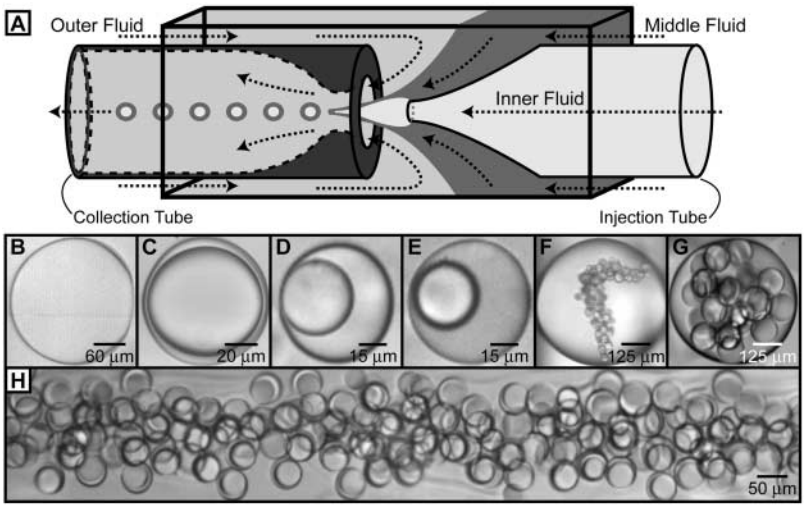

Fig. 1. Microcapillary geometry for generating double emulsions from coaxial jets. (**A**) Schematic of the coaxial microcapillary fluidic device. The geometry requires the outer fluid to be immiscible with the middle fluid and the middle fluid to be in turn immiscible with the inner fluid. The geometry of the collection tube (round tube on the left) can be a simple cylindrical tube with a constriction, as shown here, or it can be tapered into a fine point (not shown). The typical inner dimension of the square tube is 1 mm; this matches the outer diameter of the untapered regions of the collection tube and the injection tube. Typical inner diameters of the tapered end of the injection tube range from 10 to 50 μm. Typical diameters of the orifice in the collection tube vary from 50 to 500 μm. (**B** to **E**) Double emulsions containing only one internal droplet. The thickness of the coating fluid on each drop can vary from extremely thin (less than 3 μm) as in (**B**) to significantly thicker. (**F** and **G**) Double emulsions containing many internal drops with different size and number distributions. (**H**) Double emulsion drops, each containing a single internal droplet, flowing in the collection tube. The devices used to generate these double emulsions had different geometries.

double emulsion with a single internal drop. These types of double emulsions can be generated when both fluids are simultaneously dripping (Fig. 2A) or simultaneously jetting (Fig. 2B) (movies S1 to S4). The dripping and jetting mechanisms are closely related, and the transition between them is induced by varying the flow rate of the outermost fluid Q_{OF}. The dripping regime occurs for lower Q_{OF}, and increasing Q_{OF} focuses the coaxial jet more strongly, thinning the inner stream, which leads initially to smaller double emulsion drops. The radius of the outer emulsion drops, R_{drop}, decreases linearly with Q_{OF} (Fig. 3, solid circles). However, increasing Q_{OF} beyond a threshold value causes the jet to abruptly lengthen, signifying the transition to the jetting regime (*36*); this results in a discontinuous increase in R_{drop} (Fig. 3, solid triangles). In contrast, the radius of the coaxial jet, R_{jet}, measured near the exit orifice decreases monotonically through the transition (Fig. 3, half-filled symbols). As a result, the frequency of droplet production decreases.

We can construct a simple physical model for these phenomena. The classic mechanism of drop formation from a cylindrical fluid thread is through the Rayleigh-Plateau instability (*37*, *38*). This instability is driven by interfacial tension and reduces the total surface area of a fluid thread by breaking it into drops. Thus, fluid cylinders are unstable to axisymmetric perturbations with wavelengths larger than several times the radius of the cylinder itself. Although this is strictly valid only for a jet made up of a single fluid, in our experiments we matched the viscosities of the innermost and middle fluids ($\eta_{IF} = \eta_{MF}$), ensuring that the velocity profile of the coaxial jet was equivalent to that of a single fluid, and we applied the same considerations to the coaxial fluid cylinder. We also assumed that the fluids are Newtonian. The growth rate of a perturbation is determined by its velocity perpendicular to the interface, $v_\perp \sim \gamma/\eta_{OF}$, where γ is interfacial tension, leading to a droplet pinch-off time of $t_{pinch} = CR_{jet}\eta_{OF}/\gamma$, where C is a constant that depends on the viscosity ratio. Numerical calculations give $C \approx 20$ when $\eta_{IF}/\eta_{OF} = 0.1$ (*39*). Again, this is strictly valid for a cylinder of a single fluid; for a coaxial fluid thread, the effective interfacial tension may be modified by the fact that there are two interfaces. However, the Rayleigh-Plateau instability cannot occur until the length of the jet has grown to be comparable to its radius. This occurs at growth time $t_g \sim R_{jet}^3/Q_{sum}$, where Q_{sum} is the net flow rate of the two inner fluids. If $t_{pinch} < t_g$, droplets will be formed as soon as the jet is large enough to sustain the instability, which will occur right at the outlet; this leads to the dripping regime (Fig. 2A). If $t_{pinch} > t_g$, the jet will grow faster than the droplets can form; this leads to the jetting regime, where the droplets are formed downstream (Fig. 2B). We thus define an effective capillary number of the interface

$$Ca = \frac{t_{pinch}}{t_g} = \frac{\eta_{OF} Q_{sum}}{\gamma R_{jet}^2} = \frac{\eta_{OF} v}{\gamma} \qquad (1)$$

where v is the downstream velocity of the inner fluids. This equation governs the transition between dripping and jetting, which occurs when $Ca \sim 1$. Expressing the control parameter in terms of a capillary number captures the physical picture that the transition from dripping to jetting occurs when viscous stresses on the interface caused by the fluid flow become so large that the Rayleigh-Plateau instability is suppressed in these tube geometries.

Based on this simple physical picture, we can determine R_{jet} and R_{drop} as a function of Q_{OF} by considering the velocity flow profiles in both regimes. However, these velocity profiles evolve as the fluids enter and move downstream through the collection tube, necessitating a different treatment for each mechanism.

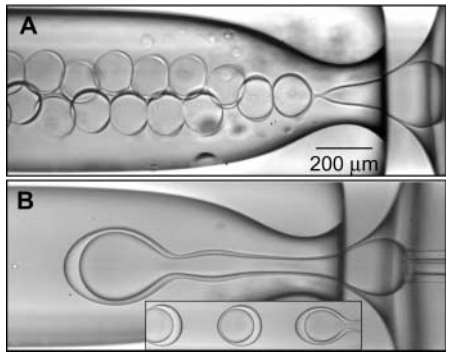

Fig. 2. Steady-state drop formation mechanisms that result in monodisperse double emulsions with a single internal droplet. (**A**) Dripping and (**B**) jetting. In both cases, the rate of drop formation is the same for the inner and middle fluids. The transition between dripping and jetting is controlled by Q_{OF} for fixed total flow rates of the inner and middle fluids. The double emulsions in (A) have a polydispersity less than 1% and those in (B) have a polydispersity of about 3%. (Inset at bottom) Pinch-off of the double emulsion drops from the coaxial jet. The same device and same fluids were used for the experiments described in Figs. 2 and 3. The outer fluid used was silicon oil with $\eta_{OF} = 0.48$ Pa·s, the middle fluid was a glycerol-water mixture with $\eta_{MF} = 0.05$ Pa·s, and the inner fluid was silicon oil with $\eta_{IF} = 0.05$ Pa·s. The interfacial tension for the aqueous mixture and silicon oil without surfactants is approximately 20 mN/m. The flow rates of the fluids in (A) are $Q_{OF} = 2500$ μl hour^{-1}, $Q_{MF} = 200$ μl hour^{-1}, and $Q_{IF} = 800$ μl hour^{-1}. The flow rates in (B) are $Q_{OF} = 7000$ μl hour^{-1}, $Q_{MF} = 200$ μl hour^{-1}, and $Q_{IF} = 800$ μl hour^{-1}. We applied these flow rates with stepper-motor–controlled syringe pumps (Harvard Apparatus, Holliston, MA).

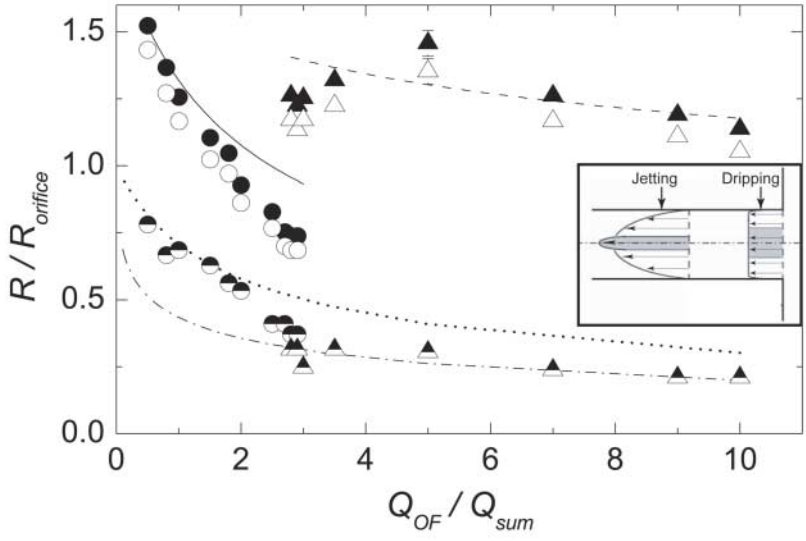

Fig. 3. Drop and jet radii versus the flow rates. The drop and jet radii are scaled by the radius of the orifice and we plotted as a function of Q_{OF}, scaled by Q_{sum}, where $Q_{sum} = Q_{MF} + Q_{IF}$. Solid circles represent the drop diameter in the dripping regime, and open circles represent the inner droplet diameter in the dripping regime. Solid triangles represent the drop diameter in the jetting regime, and open triangles represent the inner droplet diameter in the jetting regime. The solid line represents the results of the model that predicts the drop size in the dripping regime, and the dashed line represents the results of the model that predicts drop size in the jetting regime. Half-filled circles represent the jet radius in the dripping regime, and half-filled triangles represent the jet radius in the jetting regime. The dotted line is the jet radius predicted for a flat velocity profile, and the dash-dotted line is the jet radius predicted for a parabolic velocity profile. The jet radius was consistently measured at the constriction in the collection tube. (Inset) The evolution of a flat velocity profile into a parabolic velocity profile. The gray core represents the coaxial jet and the labels show the drop formation mechanism that is associated with each velocity profile. For all of the experiments, Q_{sum} was fixed at 1000 μl hour^{-1} and Q_{IF}/Q_{MF} was fixed at 4.

When the coaxial jet first enters the exit orifice, the velocity profile of the fluids is approximately flat across the channel (Fig. 3, inset). It remains this way for a distance comparable to the orifice radius times the Reynolds number. Thus, in the dripping regime, where drops form very close to the orifice, mass flux is related to cross-sectional area

$$\frac{Q_{sum}}{Q_{OF}} = \frac{\pi R_{jet}^2}{\pi R_{orifice}^2 - \pi R_{jet}^2} \quad (2)$$

where $R_{orifice}$ is the radius of the exit orifice. The values of $R_{jet}/R_{orifice}$ predicted from Eq. 2, with no adjustable parameters, are in good agreement with the measured values in the dripping regime (Fig. 3, dotted line). Comparison of the measured radii of the drops and the coaxial jet shows that $R_{drop} = 1.87\ R_{jet}$. This empirical relationship is consistent with theoretical calculations (*40*) of R_{drop} for the breakup of an infinitely long cylindrical thread in an ambient fluid for $\eta_{IF}/\eta_{OF} = 0.1$. From this we can predict R_{drop}, which is in good agreement with the data (Fig. 3, solid line). The small discrepancy near the transition probably results from deviation from a flat velocity profile.

In the jetting regime, where drops are formed well downstream, the fluid flow has evolved into the classic parabolic velocity profile of laminar pipe flow. The viscosity difference between the fluids causes the inner coaxial jet to develop a different velocity profile from that of the outer fluid. The full profiles can be determined by solving the Navier-Stokes equations in the low Reynolds number limit (SOM text II). The jet expands slightly as the collection tube widens, modifying the flow profiles; therefore, we assume a constant radius and determine the dependence of the fluid flow rates on the viscosities and $R_{jet}/R_{orifice}$ (eq. S1). We can thus predict the jet radii using no adjustable parameters, and obtain good agreement with values measured before the jet has expanded (Fig. 3, dashed-dotted line).

Drop formation in the jetting regime is generally irregular, leading to more polydisperse size distribution. However, quite stable droplet formation can be achieved, occurring at a fixed location on the jet. We believe that this condition occurs because of the geometry of our collection tube, whose diameter rapidly expands after the narrow orifice. This leads to an expansion of the jet diameter and a concomitant decrease in the velocity. As soon as *Ca* decreases sufficiently to sustain the Rayleigh-Plateau instability, droplets rupture, fixing the location and resulting in quite monodisperse droplets. In the jetting regime, the frequency of rupture decreases, producing droplets that are quite a bit larger than the size of the jet (Fig. 3). It takes time to fill these larger drops, and we can use mass conservation of the dispersed phases and the characteristic time scale for drop breakoff to obtain $Q_{sum} = (4/3)\pi R_{drop}^3/t_{pinch}$. Solving for drop radius gives,

$$R_{drop} = \left(\frac{15 Q_{sum}}{\pi} \frac{R_{jet}\eta_{OF}}{\gamma}\right)^{1/3} \quad (3)$$

This prediction yields excellent agreement with our results, as shown by the dashed line in Fig. 3. Again, there is some discrepancy between the model and data in the region of the transition, which is not described by Eq. 3. However, the predictive capability of these models provides important guidance in creating double emulsions of a desired size.

The ability to produce precision double emulsions creates many opportunities to fabricate new materials. We can control all three flow rates independently, which allows us to vary the number of internal droplets and the shell thickness. In addition, the inner and outer fluids never come into contact, facilitating great flexibility in devising schemes for encapsulation. One of the major benefits of this technique is the ability to fabricate core-shell structures, and these can easily be made into capsules. As an illustrative example, we fabricated a rigid spherical shell by photopolymerizing a polymer [Norland Optical Adhesive (NOA), Norland Products, Cranbury, NJ] in the middle fluid. We diluted the adhesive by 30% with acetone to decrease its viscosity. After generating the double emulsions, we cured the shells with an ultraviolet (UV) light source for approximately 10 s as the double emulsions traversed the collection tube. Brightfield images of the double emulsions and the resulting solid shells are shown in Fig. 4, A and B, respectively. To confirm that we indeed formed solid shells, we crushed the spheres between two microscope cover slides. A scanning electron micrograph (SEM) image confirmed the cracked polymer shells (Fig. 4C).

We can also use our device to make polymer vesicles, or polymerosomes (*41*). We created double emulsions with a single internal drop and dissolved diblock copolymers in the intermediate fluid. We used a volatile fluid as the intermediate phase and subsequently evaporated it, thereby forming polymerosomes. This method is a modified solvent evaporation technique (*15*) and is similar to a technique that has been used to produce solid polymer spheres from double emulsions (*14–16*, *19–21*). Because we can precisely control the double emulsion drop morphology, we can produce highly controllable polymerosomes. To illustrate this, we generated water-in-oil-in-water double emulsions, with a middle fluid composed of 70% toluene and 30% tetrahydrofuran (THF). This middle fluid serves as the carrier for a diblock copolymer, poly(butyl acrylate)-b-poly(acrylic acid) (PBA-PAA) (Fig. 4D) (*42*). As the solvent evaporates, the amphiphilic polymers self-assemble into layers on both interfaces, forming polymerosomes. The concentrations of the diblocks were not precisely adjusted; thus, the polymerosomes were not strictly unilamellar. However, the polymer bilayers were very thin, making it difficult to resolve them in brightfield microscopy. Thus, a phase-contrast image of a typical polymer vesicle is shown in Fig. 4E. To confirm that these structures are indeed polymerosomes, we deflated them with osmotic stress by adding a sucrose solution (0.1 M) to the continuous fluid. The polymerosome from Fig. 4E deflated in this way is shown in Fig. 4F. This

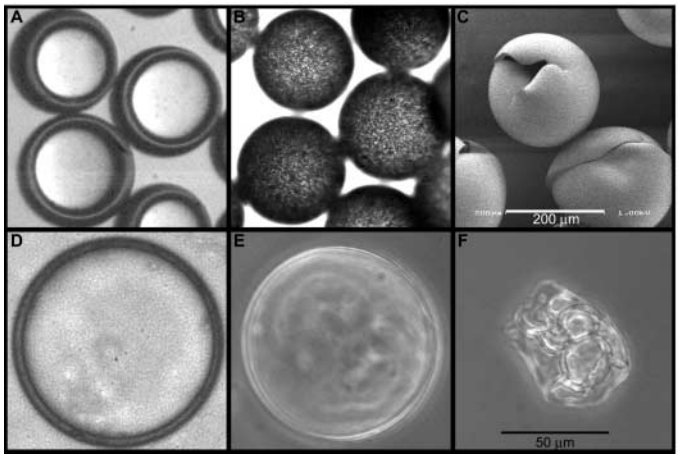

Fig. 4. Core-shell structures fabricated from double emulsions generated in our device. (**A**) Optical photomicrograph of the water-in-oil-in-water double emulsion precursor to solid spheres. The oil consists of 70% NOA and 30% acetone, with a viscosity of approximately 50 mPa·s. (**B**) Optical photomicrograph of rigid shells made by cross-linking the NOA by exposure to UV light. (**C**) SEM of the shells shown in (B) after they have been mechanically crushed. The scale bar in (C) also applies to (A) and (B). (**D**) Brightfield photomicrograph of the water-in-oil-in-water double emulsion precursor to a polymer vesicle. The oil phase consists of a mixture of toluene and tetrahydrofuran at 70/30 v/v with dissolved diblock copolymer (PBA-PAA) at 2% w/v. The viscosity of this mixture was approximately 1 mPa·s. (**E**) Phase-contrast image of the diblock copolymer vesicle after evaporation of the organic solvents. (**F**) Phase-contrast image of the deflated vesicle after osmotic stress was applied through the addition of 0.1 M sucrose to the outer fluid. The scale bar in (F) also applies to (D) and (E).

technique has a sizeable advantage: The inner and outer fluids remain totally separate, providing for efficient and robust encapsulation. In addition to polymerosomes, it should also be possible to form liposomes from phospholipids in the same manner. Alternatively, other methods to produce robust encapsulants include surface-induced polymerization of either the inner or outer interface or temperature-induced gelation of the inner or middle fluid.

Our microcapillary fluidic device is truly three dimensional, completely shielding the inner fluid from the outer one. It can generate double emulsions dispersed in either hydrophilic or hydrophobic fluids. Its production of double emulsion droplets is limited by the drop formation frequency, which varies between approximately 100 and 5000 Hz. Increasing the production rate requires the operation of parallel devices; for this, a stamping technique (*43*) would be highly desirable. However, an operational device would require control of the wetting properties of the inner channels. Alternatively, a hybrid device incorporating capillary tubes into the superstructure may offer an alternate means of making devices to produce double emulsions.

References and Notes

1. K. J. Lissant, *Emulsion and Emulsion Technology* (Marcel Dekker, New York, 1974), vol. 6.
2. C. Laugel, A. Baillet, M. P. Y. Piemi, J. P. Marty, D. Ferrier, *Int. J. Pharm.* **160**, 109 (1998).
3. C. Laugel, P. Rafidison, G. Potard, L. Aguadisch, A. Baillet, *J. Controlled Release* **63**, 7 (2000).
4. M. Gallarate, M. E. Carlotti, M. Trotta, S. Bovo, *Int. J. Pharm.* **188**, 233 (1999).
5. B. Raghuraman, N. Tirmizi, J. Wiencek, *Environ. Sci. Technol.* **28**, 1090 (1994).
6. A. Edris, B. Bergnstahl, *Nahrung/Food* **45**, 133 (2001).
7. A. Benichou, A. Aserin, N. Garti, *Polym. Adv. Technol.* **13**, 1019 (2002).
8. N. Vasishtha, H. W. Schlameus, *Microencapsulation of Food Ingredients*, P. Vilstrup, Ed. (Leatherhead Food International, Leatherhead, UK, 2001).
9. D. Lee *et al.*, *J. Dispersion Sci. Technol.* **23**, 491 (2002).
10. M. Lee, S. Oh, S. Moon, S. Bae, *J. Colloid Interface Sci.* **240**, 83 (2001).
11. V. Muguet *et al.*, *J. Controlled Release* **70**, 37 (2001).
12. S. Omi, K. Katami, T. Taguchi, K. Kaneko, M. Iso, *J. Appl. Polym. Sci.* **57**, 1013 (2003).
13. L-Y. Chu *et al.*, *J. Colloid Interface Sci.* **265**, 187 (2003).
14. R. Alex, R. Bodmeier, *J. Microencapsul.* **7**, 347 (1990).
15. S. Cohen, T. Yoshioka, M. Lucarelli, L. H. Hwang, R. Langer, *Pharm. Res.* **8**, 713 (1991).
16. N. Nihant, C. Schugens, C. Grandfils, R. Jérôme, P. Teyssié, *Pharm. Res.* **11**, 1479 (1994).
17. R. Cortesi, E. Esposito, G. Luca, C. Nastruzzi, *Biomaterials* **23**, 2283 (2002).
18. A. Lamprecht, H. Yamamoto, H. Takeuchi, Y. Kawashima, *J. Controlled Release* **98**, 1 (2004).
19. H. K. Kim, T. G. Park, *J. Controlled Release* **98**, 115 (2004).
20. M. Chiba, J. Hanes, R. Langer, *Biomaterials* **18**, 893 (1997).
21. Y. Yamaguchi *et al.*, *J. Controlled Release* **81**, 235 (2002).
22. C. Goubault *et al.*, *Langmuir* **17**, 5184 (2001).
23. S. Okushima, T. Nisisako, T. Torii, T. Higuchi, *Langmuir* **20**, 9905 (2004).
24. I. G. Loscertales *et al.*, *Science* **295**, 1695 (2002).
25. M. F. Ficheux, L. Bonakdar, F. Leal-Calderon, J. Bibette, *Langmuir* **14**, 2702 (1998).
26. R. Mezzenga, B. M. Folmer, E. Hughes, *Langmuir* **20**, 3574 (2004).
27. J. Jiao, D. G. Rhodes, D. J. Burgess, *J. Colloid Interface Sci.* **250**, 444 (2002).
28. K. Pays, J. Giermanska-Kahn, B. Pouligny, J. Bibette, F. Leal-Calderon, *Phys. Rev. Lett.* **87**, 178304 (2001).
29. L. Wen, K. D. Papadopoulos, *J. Colloid Interface Sci.* **235**, 398 (2000).
30. C. H. Villa, L. B. Lawson, Y. Li, K. D. Papadopoulos, *Langmuir* **19**, 244 (2003).
31. H. González-Ochoa, L. Ibarra-Bracamontes, J. L. Arauz-Lara, *Langmuir* **19**, 7837 (2003).
32. S. L. Anna, N. Bontoux, H. A. Stone, *Appl. Phys. Lett.* **82**, 364 (2003).
33. I. Cohen, H. Li, J. L. Hougland, M. Mrksich, S. R. Nagel, *Science* **292**, 265 (2001).
34. B. Ambravaneswaran, H. J. Subramani, S. D. Phillips, O. A. Basaran, *Phys. Rev. Lett.* **93**, 034501 (2004).
35. C. Clanet, J. C. Lasheras, *J. Fluid Mech.* **383**, 307 (1999).
36. The exact value of the flow rate at which this transition occurs will depend on the details of the tube geometry.
37. J. Plateau, *Acad. Sci. Bruxelles Mem.* **23**, 5 (1849).
38. L. Rayleigh, *Proc. R. Soc. London* **29**, 71 (1879).
39. T. R. Powers, D. Zhang, R. E. Goldstein, H. A. Stone, *Phys. Fluids* **10**, 1052 (1998).
40. S. Tomotika, *Proc. R. Soc. London Ser. A* **150**, 322 (1935).
41. B. M. Discher *et al.*, *Science* **284**, 1143 (1999).
42. PBA-PAA has a molecular weight of 5500 g/mol with the hydrophobic block (PBA) making up 70% of the total molecular weight.
43. G. M. Whitesides, A. D. Stroock, *Phys. Today* **54**, 42 (2001).

44. We thank M. P. Brenner, G. Cristobal, M. Joanicot, M. Abkarian, I. Cohen, and S. Paruchuri for helpful discussions and comments. This work was supported by NSF (grant DMR-0243715), the Harvard Materials Research Science and Engineering Center (grant DMR-0213805), Rhodia, and Unilever.

Supporting Online Material

www.sciencemag.org/cgi/content/full/308/5721/537/DC1
SOM Text
Fig. S1
Movies S1 to S4

27 December 2004; accepted 8 March 2005
10.1126/science.1109164

Retreating Glacier Fronts on the Antarctic Peninsula over the Past Half-Century

A. J. Cook,[1]* A. J. Fox,[1] D. G. Vaughan,[1] J. G. Ferrigno[2]

The continued retreat of ice shelves on the Antarctic Peninsula has been widely attributed to recent atmospheric warming, but there is little published work describing changes in glacier margin positions. We present trends in 244 marine glacier fronts on the peninsula and associated islands over the past 61 years. Of these glaciers, 87% have retreated and a clear boundary between mean advance and retreat has migrated progressively southward. The pattern is broadly compatible with retreat driven by atmospheric warming, but the rapidity of the migration suggests that this may not be the sole driver of glacier retreat in this region.

Recent changes in the Antarctic ice sheet have been caused by many different drivers, including Holocene climatic change (*1*), increasing precipitation (*2*), and changing ocean temperatures (*3*). Recent regional climate change has also begun to have a direct and immediate effect on marginal parts of the ice sheet. One notable area is the Antarctic Peninsula, where climate has warmed by ~2°C since the 1950s (*4*). Retreat of ice shelves is already well underway (*5*) with retreat of 10 ice shelves during the latter part of the 20th century (*6*–*13*). Antarctic Peninsula glaciers drain a large volume of ice, although this flux is largely balanced by snow accumulation. However, the loss of ice shelves has caused acceleration of the glaciers that fed them (*14*, *15*), creating locally high imbalances. Removal of other areas of floating ice could further increase this imbalance and thus make a substantial contribution to sea level rise.

As part of a wider project funded by the U.S. Geological Survey that will record coastal change for the whole continent (*16*, *17*), we compiled maps describing changes in the ice sheet margin around the Antarctic Peninsula. The detailed cartography, including changes in glaciers and ice shelves, will be published as maps (*18*, *19*) and as digital data (*20*). Here, we present an analysis of this comprehensive time-series data set describing the extent of the 244 marine glaciers draining the Antarctic Peninsula ice sheet and those on associated islands. All of these glaciers calve directly into the sea but comprise both tidewater glaciers and glacier ice shelves (*21*). We excluded composite ice shelves from the study because their behavior is already well documented.

The data sources (table S1) used to compile the maps included over 2000 aerial photographs dating from 1940 to 2001 and more than 100 satellite images from the 1960s onward (the example in Fig. 1 is of

[1]British Antarctic Survey, Natural Environment Research Council, Madingley Road, Cambridge CB3 0ET, UK. [2]U.S. Geological Survey, 926A National Center, 12201 Sunrise Valley Drive, Reston, VA 20192–0002, USA.

*To whom correspondence should be addressed. E-mail: acook@bas.ac.uk